Electronic Supplementary Information (ESI) for Chemical Communications This journal is (c) The Royal Society of Chemistry 2024

Sandwich–structured Fe_3O_4@C@$MoSe_2$ architecture for efficient lithium ion storage

Linan Yang,[a] Chengjie Zhang,[a] Liuyang Cao,[a] Rong Xu,[a] Hongbo Li,[b] Zhanjun Yang,[a,*] Juan Li[a,*]

[a] *School of Chemistry and Chemical Engineering, Yangzhou University, Yangzhou 225002, P.R. China*

[b] *School of Chemistry and Chemical Engineering, Yancheng Institute of Technology, Yancheng 224051, P. R. China.*

Experimental

Materials and Reagents. All of the electrolytes and Whatman glass fiber (GF/D) were sourced from DodoChem Co., Ltd. Ferric chloride ($FeCl_3$), ammonium hydroxide ($NH_3 \cdot H_2O$), resorcin, selenium powder, sodium hydroxide (NaOH), formaldehyde solution (37 wt%), metallic lithium foil, hydrochloric acid (HCl), $Na_2MoO_4 \cdot 2H_2O$, ethylenediamine (EDA) and ammonia ($N_2H_4 \cdot H_2O$) were purchased from Shanghai Sinopharm Co., Ltd. No further processing was applied to any of the chemicals.

Instruments. Polycrystalline powder X-ray diffractometer (XRD, D8 Advance, Bruker AXS, Germany) was used to characterize the crystal structure of the materials. The morphology and size of the materials were acquired using scan electron microscopy (SEM, Zeiss-Supra 55, 15.0 kV). Transmission electron microscopy (TEM, JEM-2100, Japan, 20 kV) and high-resolution transmission electron microscopy (HRTEM, Tecnai G2 F30 S-TWIN, 300 kV) were employed to further obtain the refined structure and element distribution information of the materials. Raman spectroscopy (Renishaw InVia, 532 nm laser) and X-ray photoelectron spectroscopy (XPS, ThermoFisher Scientific ESCALAB250Xi, America, Al/Mg Kα) were applied

for obtain the chemical structure, elemental composition and valence states information of the materials. And the XPS tests have a limit energy resolution of 0.43 eV, and the energy analysis range is 0-5000 eV. The specific surface area and pore size distribution were collected with N_2 adsorption analyzer (ASAP 2020 HD88). Thermogravimetric analysis (TGA) tests were conducted on a TGA analyzer (Pyris 1, TGA) with a heating rate of 10 ℃ min^{-1} in an air atmosphere.

Preparation of yolk-shell Fe_3O_4@C nanocubes. α-Fe_2O_3 nanocubes were firstly synthesized by the following process. NaOH aqueous solution (50 mL, 5.4 mol/L) and $FeCl_3$ aqueous solution (50 mL, 2.0 mol/L) were prepared, and then mix in an oil bath at 75℃. After mixing, the resulting $Fe(OH)_3$ gels are poured into two 100 mL high-pressure reactors and heated at 100℃ for 48 h. When the reaction is over, water and ethanol were centrifuged alternately until the yellow solution disappears and the red products were obtained. Finally, the α-Fe_2O_3 nanocubes products were dried in a vacuum drying oven at 60℃ for 12 h.

The 80 mg of α-Fe_2O_3 nanocubes, 13 mL of water and 6 mL of $N_2H_4 \cdot H_2O$ (25 wt%) were evenly dispersed in 140 mL of ethanol under ultrasonic, then poured into 250 mL flask and stirred at 30℃. Then 30 mg of resorcin and 64 μL of formaldehyde solution were added, and stirred for 24 h. After the reaction, the precipitations were collected by centrifugation and dried in a vacuum drying oven at 60℃ for 12 h. Then, the samples were annealed at 700℃ for 3 h in Ar atmosphere. The products were etched with 40 mL of HCl (4 mol/L) for 30 min, rinsed several times in the same way as above, and finally moved to a vacuum drying oven at 60℃ for 12 h.

Preparation of sandwich–structured Fe_3O_4@C@$MoSe_2$ architecture. 0.16 g of selenium powder was added to 10 mL of hydrazine hydrate and stirred at 25℃ for 5 h to obtain solution A. 0.24 g of $Na_2MoO_4 \cdot 2H_2O$ was added to 50 mL of deionized water to acquire solution B. Under stirring conditions, solution A was added to solution B and stirred for 0.5 h. Then 5 mL of EDA was added to the above mixed solution, and continued stirring for 0.5 h, then adding 30 mg of yolk-shell Fe_3O_4@C with ultrasonic processing for 1 h. Finally, the solution was transferred to a high-pressure reactor and reacted at 200℃ for 24 h. After the reaction was cooled to room temperature, the

precipitation was centrifuged, washed, collected, and dried in vacuum at 60℃. Finally, the composite material sandwich–structured Fe_3O_4@C@$MoSe_2$ architecture was obtained by calcination at 700℃ under the protection of Ar for 2 h.

On the basis of the above preparation, step (3) was omitted, and yolk-shell Fe_3O_4@C was used as one of the contrast materials. Then the core-shell Fe_3O_4@C was etched to form a hollow C box. And in step (3), the core-shell Fe_3O_4@C was replaced by a hollow C box, and the C@$MoSe_2$ material was prepared as another contrast material.

Electrochemical measurements. Using N-Methyl-2-pyrrolidone (NMP) as solvent, sandwich–structured Fe_3O_4@C@$MoSe_2$, acetylene black and polyvinylidene difluoride (PVDF) were mixed and ground evenly according to the mass ratio of 7:2:1, and then stirred for 24 h to prepare the slurry. The resultant slurry was evenly coated on the copper foil by a coater and kept at 80℃ for 10 h. After coating, the circular electrode sheet was cut into an electrode with a diameter of 1.6 cm by cutting machine. Then the cut electrode was transferred to a vacuum drying oven and dried it at 120℃ for 12 h to remove solvent. The average areal loading amount of the active material is around 1.25 mg cm^{-2}. Finally, the electrodes were weighed and the 2032-type Coin cells were assembled in a glove box filled with Ar, and then were left to rest for 8 h. Xinwei (CT-3008W) high-performance detection system was used to carry out galvanostatic discharge-charge test in voltages range from 0.01 to 3.00 V (vs. Li/Li^+). The cyclic voltammetry (CV) characteristic curve and electrochemical impedance (EIS) of the battery were tested by Chenhua electrochemistry workstation. In CV test, voltage range was set as 0.01-3 V and scanning rate as 0.2 mV s^{-1}. The scanning frequency range of EIS test was 0.01-100 KHz, and the voltage amplitude was of 5 mV.

Effect of the amount of molybdenum source on the structure morphology of sandwich–structured Fe_3O_4@C@$MoSe_2$ architecture.

In the process of synthesizing **s**andwich–structured Fe_3O_4@C@$MoSe_2$ architecture, adding 1 mM molybdenum source can realize the uniform growth of $MoSe_2$ on the surface of Fe_3O_4@C (Fig. S1b). As shown in the Fig. S1, when the molybdenum source added is 0.5 mM (a), the growth of $MoSe_2$ nanosheets on some

Fe_3O_4@C surfaces is small and uneven, while when the molybdenum source added is 1.5 mM (c), a large number of $MoSe_2$ nanosheets self-aggregate.

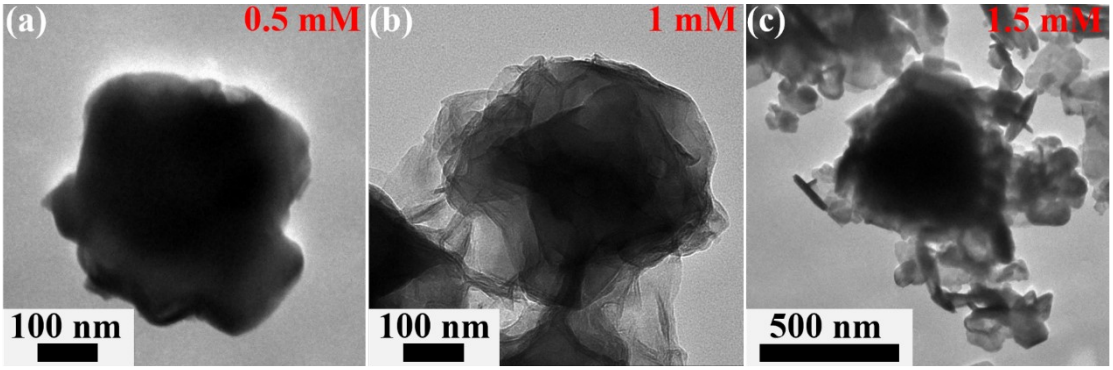

Figure S1. TEM images of the **s**andwich–structured Fe_3O_4@C@$MoSe_2$ architecture are synthesized by adding (a) 0.5 mM, (b) 1 mM and (c) 1.5 mM molybdenum source.

The morphology of the contrast material

In order to clarify the role of Fe_3O_4 core, the comparative material C@$MoSe_2$ was prepared, that is, $MoSe_2$ was coated on the carbon box with all Fe_3O_4 being fully removed. Fig. S2a shows the hollow carbon nanocubes obtained after complete etching. Its size is about 400 nm, and the wall thickness is about 20 nm. Using the same method, $MoSe_2$ nanosheets could be coated onto hollow carbon box shell (Fig. S2b). However, different from the sandwich–structured Fe_3O_4@C@$MoSe_2$, the outer $MoSe_2$ nanosheets of C@$MoSe_2$ present a state of agglomeration, which is not beneficial to electrolyte infiltration and e^-/ion transmission.

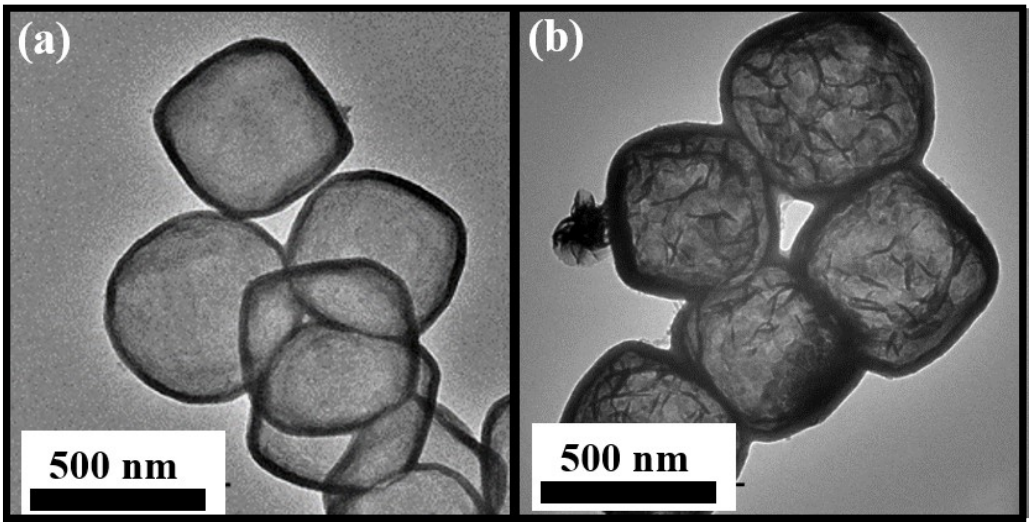

Figure S2. TEM images of (a) hollow C box and (b) C@$MoSe_2$.

Thermogravimetric analysis of sandwich–structured Fe_3O_4@C@$MoSe_2$ and yolk-shell Fe_3O_4@C.

As shown in Fig. S3, the carbon content in the yolk-shell Fe_3O_4@C is about 2.36 wt%, as determined by TGA analysis (Oxidation of the very small amount of Fe_3O_4 in the interior is ignored.). Moreover, the content of the outer coated $MoSe_2$ is calculated as 44.19 wt% through the TG of sandwich–structured Fe_3O_4@C@$MoSe_2$. The following equation is the specific calculation process.

$$2MoSe_2 + 7O_2 = 2MoO_3 + 4SeO_2\uparrow \#(1)$$

m ($MoSe_2$) = m (SeO_2) * M ($MoSe_2$)/ M (SeO_2) / 2 = (40.99-2.36) * 253.87 / 110.96 /2 wt% = 44.19 wt%

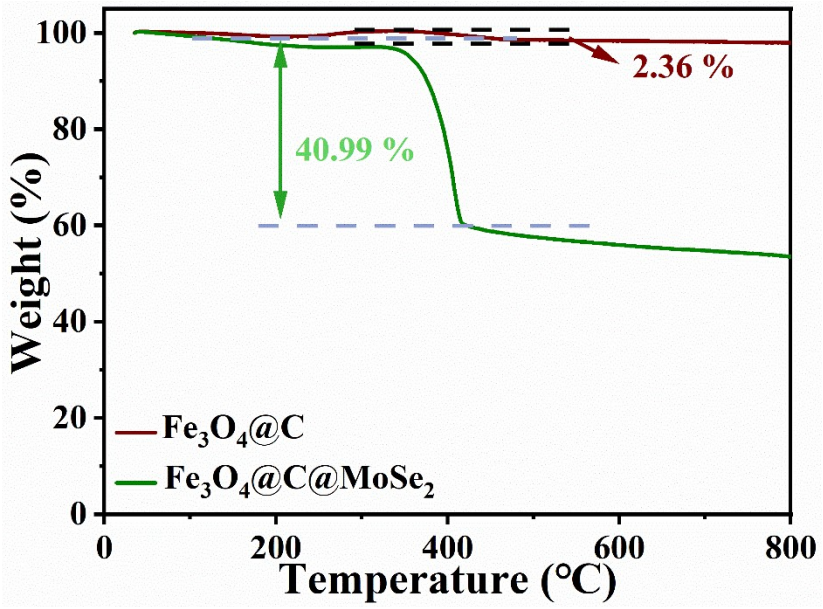

Figure S3. TGA of sandwich–structured Fe_3O_4@C@$MoSe_2$ and yolk-shell Fe_3O_4@C.

N_2 isothermal adsorption/desorption measurements of sandwich–structured Fe_3O_4@C@$MoSe_2$ and yolk-shell Fe_3O_4@C.

Furthermore, according to N_2 isothermal adsorption/desorption measurements (Fig. S4a, ESI†), the specific surface area of Fe_3O_4@C@$MoSe_2$ (32.59 m^2 g^{-1}) is higher than that of Fe_3O_4@C (12.93 m^2 g^{-1}). And the pore size distribution curve (Fig. S4b, ESI†) shows that both of them have mesoporous structures. But the total pore volume of Fe_3O_4@C@$MoSe_2$ (1.23×10^{-1} cm^3 g^{-1}) is larger than that of Fe_3O_4@C (8.97×10^{-2} cm^3

g^{-1}), and the former has a larger average pore size. The increased surface area and abundant mesoporous structure provide sufficient channels for Li^+/e^- migration, and alleviate the significant volume change during charge/discharge, improving electrode stability.

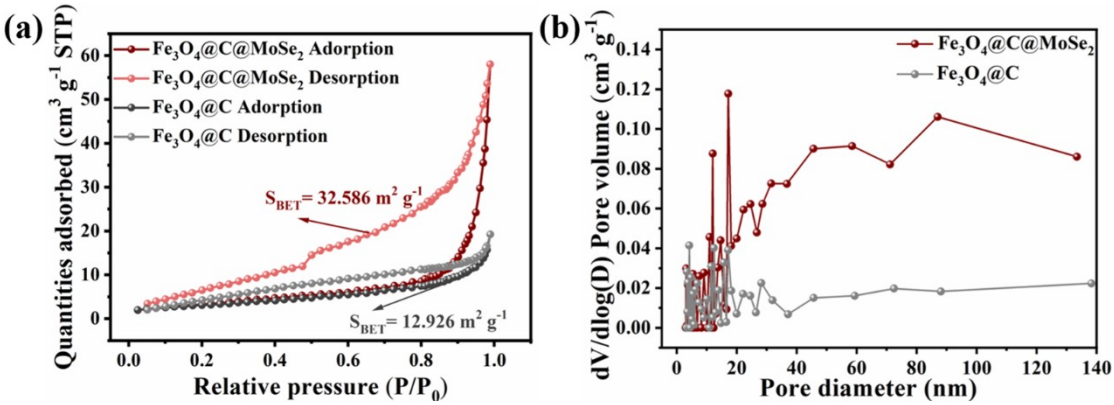

Figure S4. (a) N_2 adsorption-desorption isotherms and (b) pore size distribution curves of yolk-shell Fe_3O_4@C and sandwich–structured Fe_3O_4@C@$MoSe_2$.

C 1s X-ray photoelectron spectra of sandwich–structured Fe_3O_4@C@$MoSe_2$ architectures.

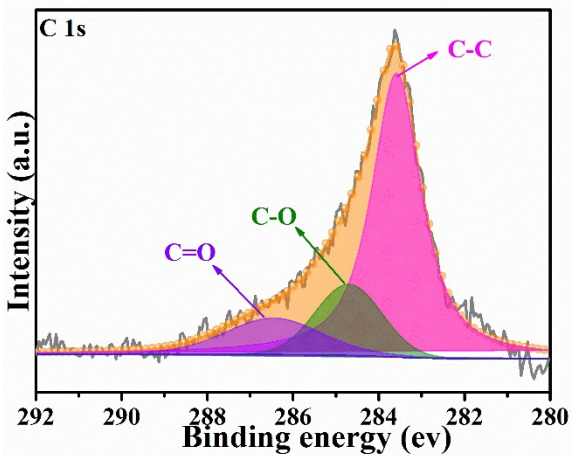

Figure S5. C 1s -XPS of sandwich–structured Fe_3O_4@C@$MoSe_2$ architectures.

Discharge/charge curves of the yolk-shell Fe3O4@C, C@MoSe2, sandwich structured Fe3O4@C@MoSe2 electrodes.

Fig. 4d-f show the discharge/charge curves of three electrodes at the first three

cycles and tenth cycle at 0.1 A g^{-1}, reflecting that test results are similar to CV curves. The Fe_3O_4@C@$MoSe_2$ electrode (Fig. 4f) shows potential plateaus at 1.8 and 0.9 V in the discharge curves, and exists a charge plateau at 2.2 V, which is consistent with CV curve. Moreover, the initial discharge/charge specific capacity of the Fe_3O_4@C@$MoSe_2$ electrode is 1397.5 and 1097.0 mAh g^{-1}, respectively, which is higher than that of C@$MoSe_2$ electrode (Fig. 4e). The initial Coulombic efficiency (CE) of the Fe_3O_4@C@$MoSe_2$ electrode (78.5%) is slightly higher than that of the C@$MoSe_2$ (77.8%). The low initial CE is mainly due to the formation of irreversible SEI film. The initial discharge/charge capacity of yolk-shell Fe_3O_4@C electrode (1836/1215 mAh g^{-1}) is higher than that of Fe_3O_4@C@$MoSe_2$ electrode, but the initial CE (66.1%) is much lower. For the conversion anode materials with poor conductivity and serious volume effect, improving the initial CE is more critical than providing capacity. Therefore, the Fe_3O_4@C@$MoSe_2$ as the anode of LIBs has higher initial CE, reversible specific capacity and cyclic stability, and shows excellent electrochemical performance.

Lithium storage mechanism discussion.

Figure S6 shows the second cycle charge-discharge curve at 0.1 A g^{-1} current density. The charge and discharge platform in the figure can show the performance mechanism of the battery charge and discharge cycle in this work, which can be expressed by the following formula:

$$MoSe_2 + xLi^+ + xe^- \rightarrow Li_xMoSe_2 \#(2)$$

$$Fe_3O_4 + xLi^+ + xe^- \rightarrow Li_xFe_3O_4 \#(3)$$

$$Li_xMoSe_2 + (4-x)Li^+ + 4e^- \rightarrow Mo + 2Li_2Se \#(4)$$

$$Li_xFe_3O_4 + (8-x)Li^+ + 8e^- \rightarrow 3Fe + 4Li_2O \#(5)$$

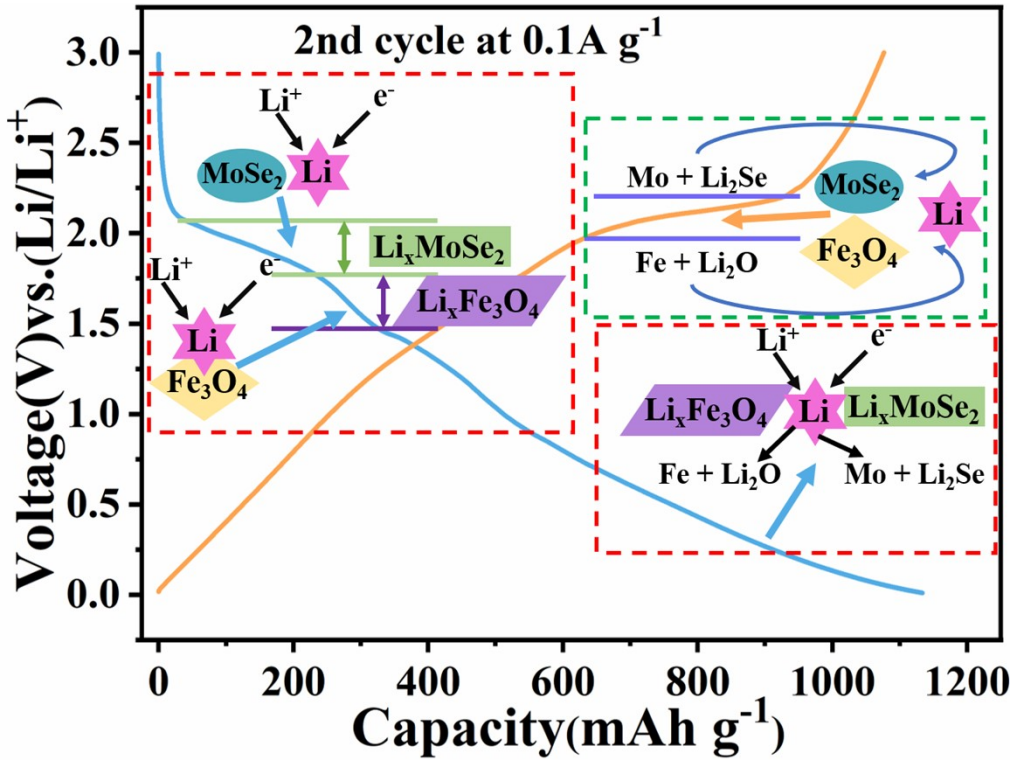

Figure S6. Charge-discharge profiles of Fe_3O_4@C@$MoSe_2$ electrode at the 2nd cycle.

A detailed analysis of the Nyquist plots.

The Nyquist plots of three electrodes measured by EIS are composed of semicircles in the high/intermediate frequency region and inclined lines in the low frequency region (Fig. 5d). The smaller the semicircle diameter, the smaller resistance, the more conducive to e^- transmission. By comparison, the semicircle diameter of Fe_3O_4@C@$MoSe_2$ composite is slightly smaller than yolk-shell Fe_3O_4@C and much smaller than C@$MoSe_2$. This indicates that the coating of $MoSe_2$ nanosheets on the surface will lead to the increase of electrode resistance. But the unique structure of the yolk-shell Fe_3O_4@C can effectively avoid the agglomeration of $MoSe_2$ nanosheets and enhance the electrical conductivity, which is conducive to the rapid transmission of e^- in the electrode to achieve faster charge transfer. The inclined line in the low frequency region corresponds to the diffusion speed of Li^+, and the larger the slope, the best Li^+ diffusion kinetics. The slope of the inclined line of Fe_3O_4@C@$MoSe_2$ electrode in the low frequency region is slightly larger than that of yolk-shell Fe_3O_4@C electrode, but

less than that of C@$MoSe_2$. This means that the presence of $MoSe_2$ nanosheets can greatly shorten the diffusion path of Li^+ and improve the diffusion ability. However, due to the presence of Fe_3O_4 core part, the ion diffusion speed of architecture is hindered. Therefore, the Fe_3O_4@C@$MoSe_2$ is an excellent electrode material which combines the advantages of Fe_3O_4, $MoSe_2$ and C.

Morphology of sandwich–structured Fe_3O_4@C@$MoSe_2$ electrode after 50 cycles.

As shown in Fig. S7, the sandwich–structured Fe_3O_4@C@$MoSe_2$ architecture can still basically maintain the sandwich–structure after 50 cycles at the current density of 0.1 A g^{-1}, and no obvious structural collapse occurs.

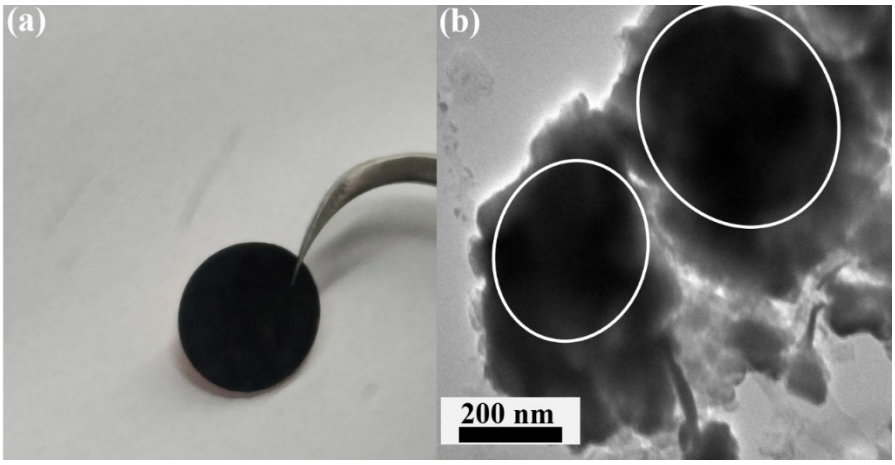

Figure S7. (a) Digital photograph and (b) TEM image of the Fe_3O_4@C@$MoSe_2$ electrode after 50 cycles at a current density of 0.1 A g^{-1}.

Table S1 Comparison of lithium storage performance of some $MoSe_2$-based anode materials.

Sample	Current density (A g^{-1})	Number of cycles	Capacity (mAh g^{-1})	Reference
$MoSe_2$ nanoflowers	0.1	200	641.4	1
MoO_2@$MoSe_2$	2	400	520.4	2
$MoSe_2$/CMK-5	0.1	100	788	3
$MoSe_2$/rGO	0.5	100	917	4
2D $MoSe_2$/rGO	0.1	100	715	5
$MoSe_2$/NC	0.2	150	86	6
MoO_2@$MoSe_2$@NC	0.5	80	468	7
NHMCFs/$MoSe_2$	1	400	586.7	8
$MoSe_2$@Ti_2N MXene	0.1	200	826	9
$MoSe_2$/C	0.1	50	576.7	10
sandwich–structured	0.1	70	876	This article
Fe_3O_4@C@$MoSe_2$	1	300	609	

References

S1 H.J. Zhang, Y.K. Wang, L.B. Kong, *Nanoscale,* 2019, **11**, 7263-7276.

S2 X. Zhao, J.H. Sui, F. Li, H.T. Fang, H.G. Wang, J.Y. Li, W. Cai, G.Z. Cao, *Nanoscale,* 2016, **8**, 17902-17910.

S3 C. Zheng, C.R. Chen, L. Chen, M.D. Wei, *J. Mater. Chem. A,* 2017, **5**, 19632-19638.

S4 Z.A. Zhang, Y. Fu, X. Yang, Y.H. Qu, Z.Y. Zhang, *ChemNanoMat,* 2015, **1**, 409-414.

S5 Z.G. Luo, J. Zhou, L.R. Wang, G.Z. Fang, A.Q. Pan, S.Q. Liang, *J. Mater. Chem. A,* 2016, **4**, 15302-15308.

S6 C. Zheng, J.X. Wu, Y.F. Li, X.J. Liu, L.X. Zeng, M.D. Wei, *ACS Sustain. Chem.*

Eng. 2021, **40**, 5514-5523.

S7 Z.X. Qin, X.L. Liu, Z.Y. Huang, R. Sun, Z.Y. Li, H.S. Fan, S.J. Lu, *Acta Metall. Sin. (Engl. Lett.),* 2021, **34**, 425-434.

S8 X.P. Ni, Z. Cui, H.X. Luo, H.F. Chen, C.L. Liu, Q.L. Wu, A.Q. Ju, *Chem. Eng. J.* 2021, **404**, 126249.

S9 H. Zong, L. Hu, Z.G. Wang, K. Yu, S.J. Gong, Z.Q. Zhu, *CrystEngComm,* 2020, **22**, 5995-6002.

S10 Y. Liu, M.Q. Zhu, D. Chen, *J. Mater. Chem. A,* 2015, **3**, 11857-11862.